Site Characterization and Site Response in Port-au-Prince, Haiti

Susan E. Hough,[a)]Alan Yong,[a)]Jean Robert Altidor,[b)]Dieuseul Anglade,[b)]Doug Given,[a)]and Saint-Louis Mildor[b)]

Waveform analysis of aftershocks of the M_w7.0 Haiti earthquake of 12 January 2010 reveals amplification of ground motions at sites within the Cul de Sac valley in which Port-au-Prince is situated. Relative to ground motions recorded at a hard-rock reference site, peak acceleration values are amplified by a factor of approximately 1.8 at sites on low-lying Mio-Pliocene deposits in central Port-au-Prince and by a factor of approximately 2.5–3 on a steep foothill ridge in the southern Port-au-Prince metropolitan region. The observed amplitude, predominant periods, variability, and polarization of amplification are consistent with predicted topographic amplification by a steep, narrow ridge. A swath of unusually high damage in this region corresponds with the extent of the ridge where high weak-motion amplifications are observed. We use ASTER (Advanced Spaceborne Thermal Emission and Reflection Radiometer) imagery to map local geomorphology, including characterization of both near-surface and of small-scale topographic structures that correspond to zones of inferred amplification. [DOI: 10.1193/1.3637947]

INTRODUCTION

The 12 January 2010 M_w7.0 Haiti earthquake caused widespread damage in Port-au-Prince as well as smaller cities closer to the mainshock rupture to the west. The extent of damage was primarily due to the proximity of the earthquake to Port-au-Prince, the high vulnerability of many structures, and the high population density. Additionally there is the expectation that shaking was amplified by local geologic structure. Port-au-Prince is situated within the Cul de Sac depression, a large rift valley extending north of the city of Port-au-Prince and eastward into the Dominican Republic (Figure 1b). Most of the valley is underlain by young and presumably low-impedance Quaternary sediments. The city of Port-au-Prince sits within the southwest corner of the valley; most of this region is underlain by Mio-Pliocene sedimentary deposits, including marl, sandstone, siltstone, and shale, in fans and low foothills. These deposits are expected to be relatively stiff compared to younger and less consolidated Quaternary deposits. However, they are expected to be characterized by lower impedance than the adjacent central mountainous core of the southern peninsula. Applying the multi-channel analysis of surface wave (MASW) method, Cox et al. (2011) determine V_{S30} values at 36 sites throughout Port-au-Prince. Their results indicate that, away from the foothills, V_{S30} estimates at sites underlain by Mio-Pliocene deposits

---

a) U.S. Geological Survey, 525 S. Wilson Avenue, Pasadena, California 91106 (hough@usgs.gov)
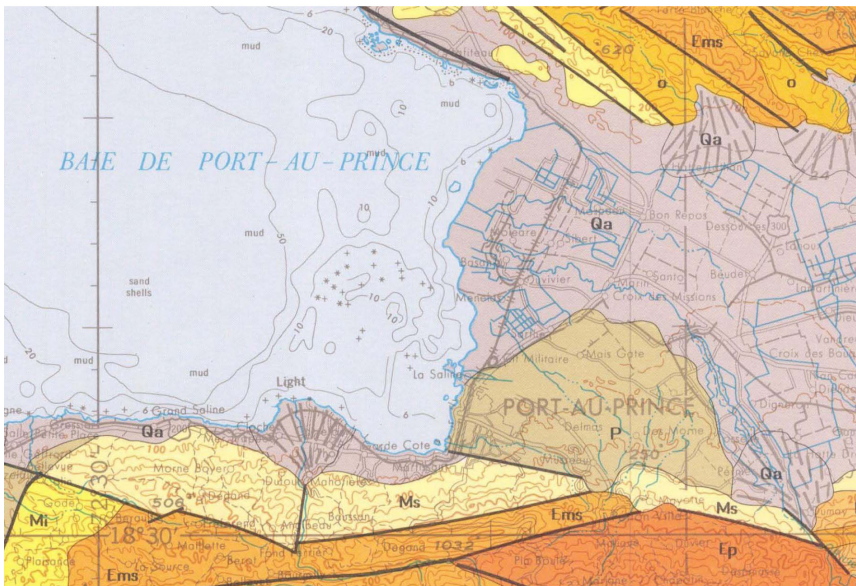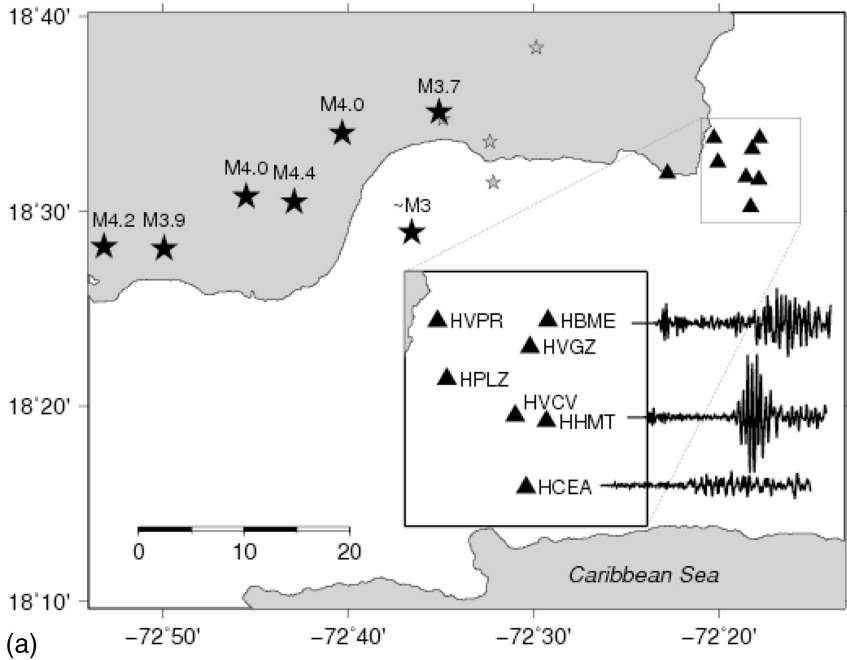b) Bureau des Mines et de l'Energie, Delmas 19, rue nina 14, Box 2174, Port-au-Prince, Haiti

Figure 1. (a) Map showing locations of K2 stations, locations of several of the larger after-shocks recorded across the array, and the NS component of ground motions for the the magnitude 3.7 aftershock on 21 March (20 March LT). (b) Geological map of Port-au-Prince region.

are in the range 360–490 m/s, corresponding to NEHRP site class C. Softer sediments, NEHRP class D, are restricted to an ~0.5–2 km wide zone along the coast.

One thus expects that some degree of amplification associated with the relatively low-impedance near-surface materials contributed to the damage within Port-au-Prince. Sediment-induced amplification has been a key factor in the distribution of damage during many recent and historical earthquakes (e.g., Borcherdt 1970, Singh et al. 1985, Hough et al. 1990). In general, sediment-induced amplification is controlled by the impedance of near-surface layers and the depth to basement, with more amplification on lower impedance soils (e.g., Borcherdt et al. 1970, Su et al. 1992, Joyner 2000, Field 2000).

No strong motion recordings of the 12 January 2010 mainshock are available. In the absence of instrumental data, macroseismic observations provide the best indication of shaking severity. For the Haiti earthquake, damage maps derived from remote-sensing imagery (http://www.dlr.de/en/desktopdefault.aspx/tabid-6213/10205_read-22076/, last accessed 10 September 2010) reveal suggestions of systematic patterns. For example, in addition to widespread damage throughout central Port-au-Prince, the distribution suggests an east-west trending band of elevated damage across the southern metropolitan region (i.e., the orange band across panel 9 in Figure 2).
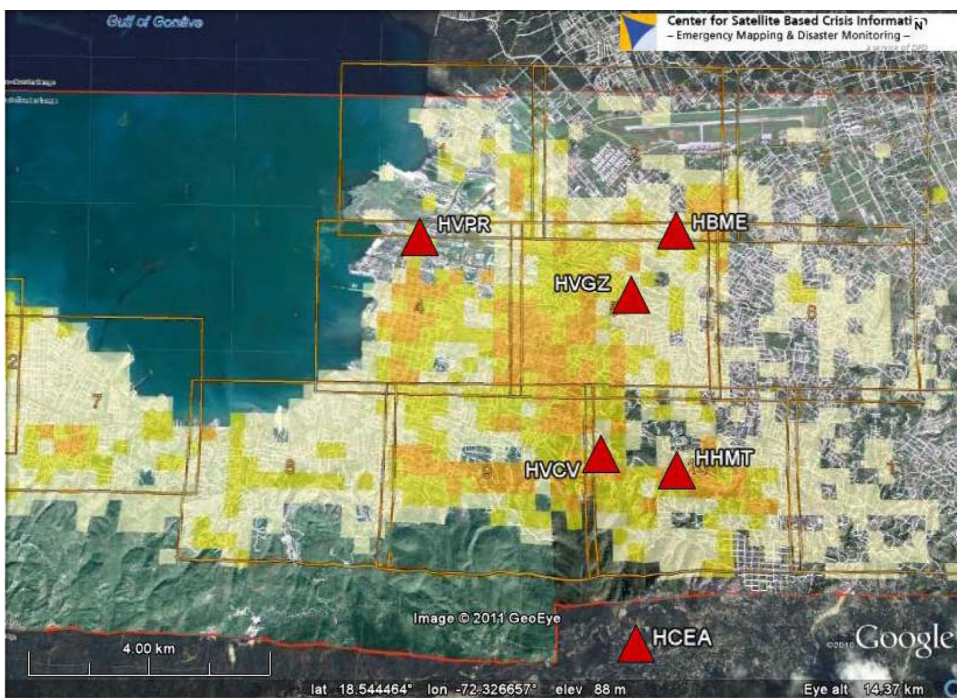

Figure 2. Damage distribution for the 12 January 2010 mainshock determined from analysis of remote-sensing imagery. Colors indicate estimated percent building damage: 0–10% (tan), 10–40% (yellow), >40% (orange). Portable seismic stations also shown (triangles): foothill stations HVCV and HHMT, reference station HCEA, and valley stations HBME, HVGZ, and HVPR.

Based on the terrain classification approach used to estimate V_{S30} values and predicted site response for USGS ShakeMaps (Allen and Wald 2009), the entire Cul de Sac Valley, including the Mio-Pliocene deposits, is essentially flat, and characterized by low V_{S30} (360–490 m/s; NEHRP Class C). However, the older deposits are not entirely flat-lying, but rather are characterized by small scale topographic variability, with elevations varying between roughly 0 and 200 m. Within this unit a conspicuous foothill ridge with higher topography runs roughly east–west through the southern Port-au-Prince metropolitan region.

A number of theoretical and observational studies have shown that topographic features, including ridges and cliff faces, can give rise to significant amplification (e.g., Hartzell et al. 1994, Spudich et al. 1996, Bouchon et al. 1996, Paolucci 2002, Assimaki et al. 2005, Lee et al. 2009), although topographic effects are generally assumed to be of less importance than sediment-induced amplification. Hough et al. (2010) present preliminary analysis of M3.5–4.5 aftershocks recorded on portable strong motion instruments deployed after the mainshock, including two (HHMT and HVCV, see Figure 1) on the crest of the foothill ridge. Hough et al. (2010) estimate weak motion peak ground acceleration (PGA) values of 2.94 +/− 1.06 for these two sites, with amplification factors reaching a factor of approximately 5 within narrow frequency bands. They show that the amplitude and predominant period of amplification are consistent with predictions for amplification associated with SH diffraction in a wedge (Sanchez-Sesma 1985). In this paper we expand on the preliminary results, analyzing additional events and considering the variability of site response at the sites on the ridge. We also develop a site characterization map for the rest of the city based on a supervised classification approach of terrain units together with available
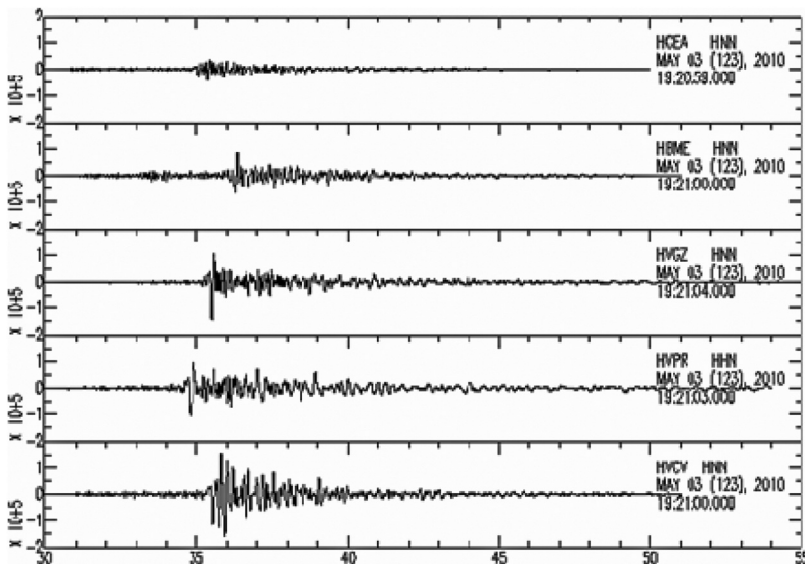

Figure 3. NS component of motion for aftershock on 3 May 2010. Time in seconds. Record from reference station HCEA is at top; record from HVCV is at bottom. Event is approximately 40 km away from the stations.

measurements of V_{S30} (Cox et al. 2011). Finally we illustrate how topographic data can be used to delineate the topographic features that are associated with observed amplification.

OBSERVED AMPLIFICATION

Weak motion amplification factors can be calculated from aftershocks recorded by nine portable K2 recorders equipped with 2 g force-balance accelerometers and, at two stations, velocity transducers (Figure 1). A description of this deployment and preliminary results are presented by Hough et al. (2010). Data can be accessed via the IRIS Data Management Center. In this paper we summarize briefly the main findings, updating the results to include data from two additional events. The deployment included a hard-rock reference site (HCEA) in the hills south of Port-au-Prince, where damage during the mainshock was limited in spite of the region's proximity to the rupture; a site on the grounds of the Hotel Montana (HHMT), a site approximately 1 km west of the Hotel Montana (HVCV), and five stations elsewhere in Port-au-Prince (Figure 1). Most of the stations remained in operation through 2010.

The high-noise urban environment necessitated high (absolute) trigger thresholds. In this paper we focus on analysis of 11 M3.3–4.5 events recorded between 21 March 2010 and 21 September 2010. These events were recorded by multiple array stations with signal-to-noise levels of a factor of 10 or higher over a frequency range 0.5–30 Hz. These events are all moreover located upwards of 30 km west of Port-au-Prince. The aperture of the array spans a distance of approximately 10 km east–west and north–south, so recordings of the same event at multiple stations will in general reflect propagation effects as well as site effects. However, stations HCEA, HHMT, HVCV, HBME, and HVGZ were deployed in a nearly north-south profile across the valley, so the distances from the stations to the aftershocks listed in Table 1 are comparable. We thus focus on analysis of these five stations, which allows us to compute and compare directly amplification at the two stations on the foothill ridge (HVCV, HHMT) with inferred amplification at two stations within the valley,

Table 1. Month (M), Day (D), origin time (hr:min:sec), and magnitude (ML) of moderate events analyzed in this study, and list of stations recording each event. Magnitude of 22 June event is estimated.

M	D	Time	ML	Stations
03	21	02:44:28	3.7	HVPR,HBME, HHMT, HCEA,HVGZ,USEM,HPKH
03	28	07:16:17	4.2	HBME,HHMT,HCEA.HVCV,HVGZ,USEM,HPKH
04	10	21:37:14	4.0	HVPR,HBME,HVCV,HVGZ,USEM,HPKH
04	11	16:32:24	3.9	HBME,HVCV,HVGZ,USEM,HPKH
05	03	05:38:48	4.0	HVPR,HCEA,HVCV,HVGZ,USEM,HPKH,HPLZ
05	03	19:21:24	4.4	HVPR,HBME,HCEA,HVCV,HVGZ,USEM,HPKH,HPLZ
05	07	21:30:04	3.6	HHMT,HCEA
05	20	06:34:09	4.4	HHMT, HPLZ, HCEA
06	22	16:06:55	3.3	HBME, HHMT, HCEA, HVCV, HPLZ
09	21	04:33:04	4.4	HBME, HHMT, HCEA, HVCV, HPKH

away from the ridge (HBME, HVGZ). Table 1 includes the full list of stations that recorded each event, for completeness.

To estimate site response at HBME, HVGZ, HVCV, and HHMT, Hough et al. (2010) calculate spectral rations relative to the reference station using smoothed spectra with a 12-sec window bracketing the S wave (both horizontal components). Spectral ratio from HBME and HVGZ are found to be indistinguishable, so results from these stations are further averaged. Hough et al. (2010) show that ground motions at all of the valley and foothill stations are systematically amplified relative to ground motions at HCEA. At HHMT the NS component of ground motion is strongly amplified at ∼6–8 Hz, with amplification in this band approaching a factor of 5. This amplification is more pronounced on the NS component than the EW component. Ground motions at HVCV are amplified more broadly over 0.5–20 Hz. Ground motions at sites in the valley, at HBME and HVGZ, are also amplified, but less dramatically, between 0.5 and ∼10 Hz.

Spectral ratios are in general characterized by high variability, which likely reflects alleatory as well as epistemic uncertainty. One potentially significant source of uncertainty is that ground motions recorded at reference station HCEA are almost certainly influenced to some extent by local site conditions (e.g., Cranswick 1988). As discussed by Hough et al. (2010), the average spectral ratios at HHMT and HVCV are only slightly above the mean +1 sigma average spectral ratio from HBME/HVGZ. To further explore site response at HHMT and HVCV we first consider the peak ground acceleration (PGA) values. On average, PGA values are amplified relative to HCEA by factors of 1.78 +/− 0.55 (1 sigma) for HBME and HVGZ, versus 2.88 +/− 1.07 for HVCV and HHMT. Considering the stations separately, PGA amplification is 3.57 +/− 0.79 at HVCV, 2.31 +/− 0.85 at HHMT, 1.75 +/− 0.36 at HBME, and 1.82 +/− 0.71 at HVGZ (Figure 4).

We also estimate PGA amplification of 2.1 +/− 0.64 for station HVPR. This site is within about 1 km of the coast, and the main port, in an area presumably underlain by soft sediments. The station recorded relatively few events due to a high trigger threshold necessitated by high noise conditions. It is also several kilometers west of the north–south
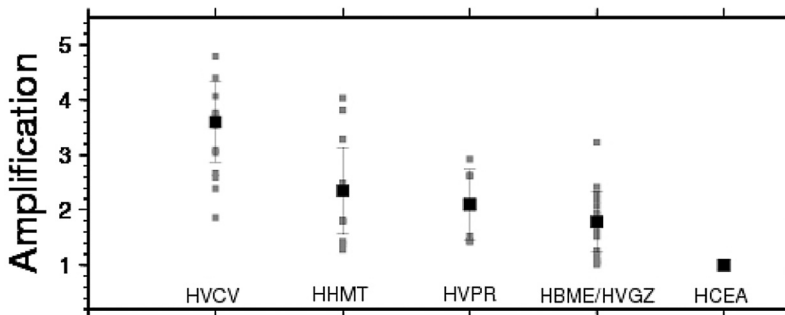

Figure 4. Average +/− 1 sigma PGA amplification factors relative to reference station HCEA (large black squares); also shown are amplification factors calculated from both horizontal components for individual events (small gray squares).

alignment of the other stations considered. Nonetheless, the estimated PGA amplification, while not well constrained, is only slightly higher than that at HBME and HVGZ.

Figure 4 reveals that, while variable, amplification factors at HVCV and HHMT reach factors of 4–5. At HHMT, the highest inferred amplifications are on the NS component. Particle motions (Figure 5) reveal strong polarization of the highest amplitude ground motions in the direction perpendicular to the ridge axis (see Figure 9). For events with relatively low values of amplification at HHMT, strong polarization is not observed.

We next consider spectrograms computed for individual events recorded at HHMT. Spectrograms are computed using one-second windows over a total time window of 10 seconds. Spectrograms from four aftershocks (Figure 6) reveal significant variability of spectral response, with a strong spectral peak around 7 Hz apparent for some events but not others. Assuming a nominal stress drop of 30 bars, one estimates source-controlled corner frequencies of roughly 5, 3, and 1.4 for magnitudes 3.3, 3.7, and 4.4. Although corner frequency and stress drop estimates are characterized by high variability (e.g., Hough 1995), the nature and variability of response suggests variability of site response rather than source properties. In particular, the site response is dominated by a strong apparent resonance around 7 Hz for some events, but not others. One of the events reveals a strong apparent resonance around 7 Hz for later arriving phases with the S-wave group, but not the initial S wave arrival (Figure 6, lower left panel).

In contrast to the variability of response at HHMT illustrated in Figure 6, the spectral response at HVCV is more consistent, with a suggested primary resonance peak around 5–6 Hz. These three events span a magnitude range of over 1 unit, with source-receiver distances range from ∼30 km to ∼80 km.

TOPOGRAPHIC AMPLIFICATION

As noted, stations HHMT and HVCV are located along the crest of a notably narrow, steep east-west trending ridges. Although topographic amplification is generally complex, an analytical solution can be derived for the simple case of SH diffraction in a wedge (Sanchez-Sesma, 1985). For a wedge with internal angle $v\pi$ and width x, a maximum amplification factor of approximately $2/v$ is predicted for frequencies $kx/\pi \sim 2$, where x is the ridge width and k is the wave number (Sanchez-Sesma 1985). The predominant frequency of amplification depends on the incidence angle. For the ridge in question, the topography is simple enough that it is illustrative to compare our observations with these predictions. The interior wedge angle is approximately 135 degrees, and the width is approximately 400 m. Assuming an average shear-wave velocity for the hill, β, of 2 km/s, one thus predicts an amplification factor of 2.7 for frequencies of ∼7 Hz. If we assume $\beta = 1$ km/s, the frequency range is reduced to ∼3.5 Hz. Cox et al. (this volume) estimate a V_{S30} value of 626 m/s at HHMT; the deeper velocity structure is unknown. (The hill is approximately 100 m high). As Sanchez-Sesma (1985) notes, higher amplifications are possible when waves reflected within the wedge interfere constructively. Using a boundary element method to investigation topographic amplification in Taiwan, Lee et al. (2009) conclude that amplifications on ridges can be as high as a factor of 2. Pischiutta et al. (2010) found amplification factors approaching a factor of 4 over the frequency range 2–4 Hz along a hill in central Italy with roughly comparable geometry. The amplitude, frequency, and polarization of the
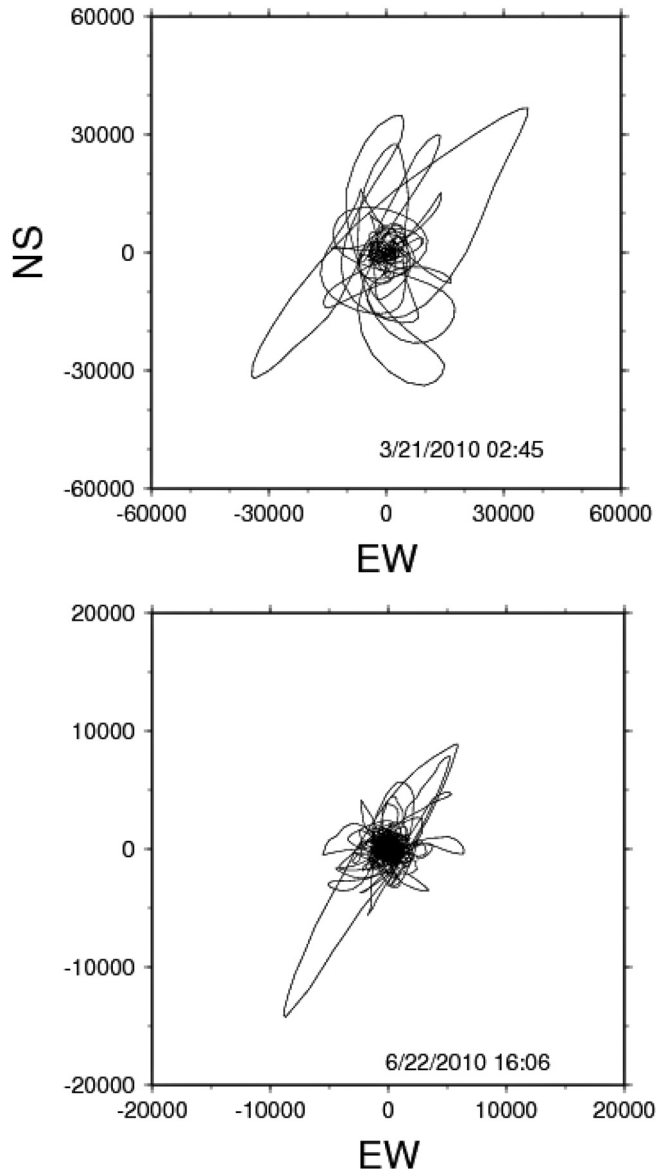
Figure 5. Particle motions for highest amplitude ground motions at HHMT for events on 21 March 2010 and 22 June 2010. The latter event had an estimated magnitude of 3.3 and a similar location as the 21 March event.

observed amplification factors at HHMT and HVCV are thus consistent with predicted topographic amplification along the ridge.

Topographic amplification is further generally expected to depend on the incident angle and potentially other characteristics of incoming waves (e.g., Sanchez-Sesma 1985,
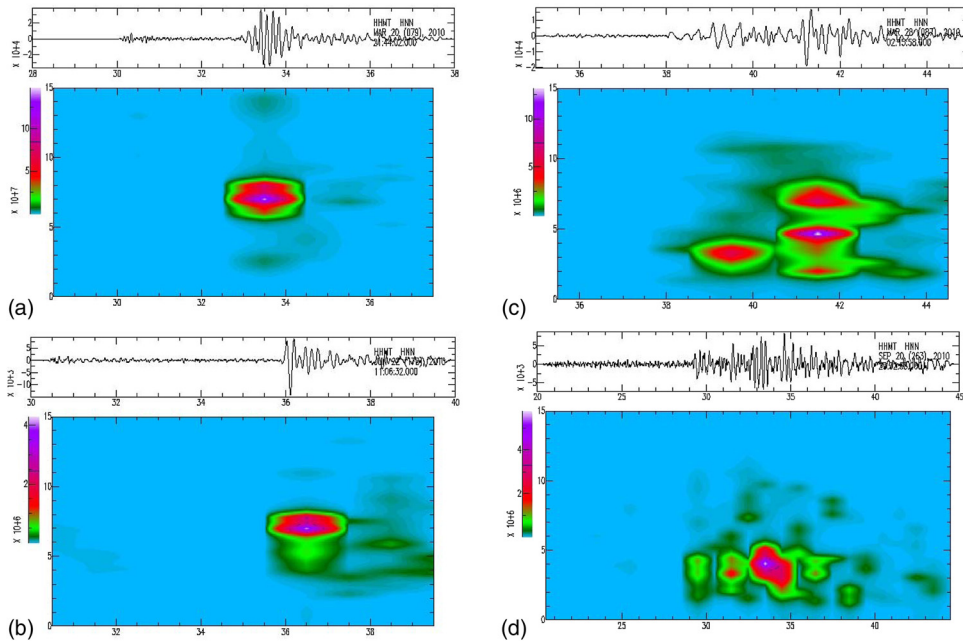
Figure 6. Spectrograms computed for the NS component at station HHMT for four aftershocks with magnitudes 3.7 (upper left), 3.3 (upper right), and 4.4 (lower two panels). Time (horizontal axes) in seconds; frequency (vertical axes) in Hz. Linear spectral amplitudes are shown, scaled by peak values in each panel.

Assimaki et al. 2005, Lee et al. 2009, Pischiutta et al. 2010). With the limited number of events well recorded across the array, it is not possible to investigate systematically the response at HHMT or HVCV as a function of source location, mechanism, etc. We speculate that the more consistent spectral response at HVCV is due to fact that, while this station is along a narrow ridge, the site is located on a small hill along the ridge, whereas HHMT is located very close to the edge of a steep edge. The high variability of amplification at station HHMT (Figure 4, Figure 6) suggests that the response of the ridge, which is particularly steep and narrow at this location, does likely vary significantly with incident angle and/or source mechanism. Sanchez-Sesma (1985) shows that the predominant frequencies associated with SH diffraction in a wedge can vary by a factor of 2, a degree of variability roughly consistent with that at HHMT.

FIRST-ORDER SITE CHARACTERIZATION

To develop a site characterization map for Port-au-Prince, and to explore the correspondence between small-scale topographic features and amplification, we consider a Digital Elevation Model derived from remote-sensing imagery. The Advance Spaceborne Thermal Emission and Reflection Radiometer (ASTER) instrument was built by Japan's METI (Ministry of Economy, Trade and Industry) and launched onboard NASA's Terra spacecraft in December 1999. It has an along-track stereoscopic capability using its near infrared spectral
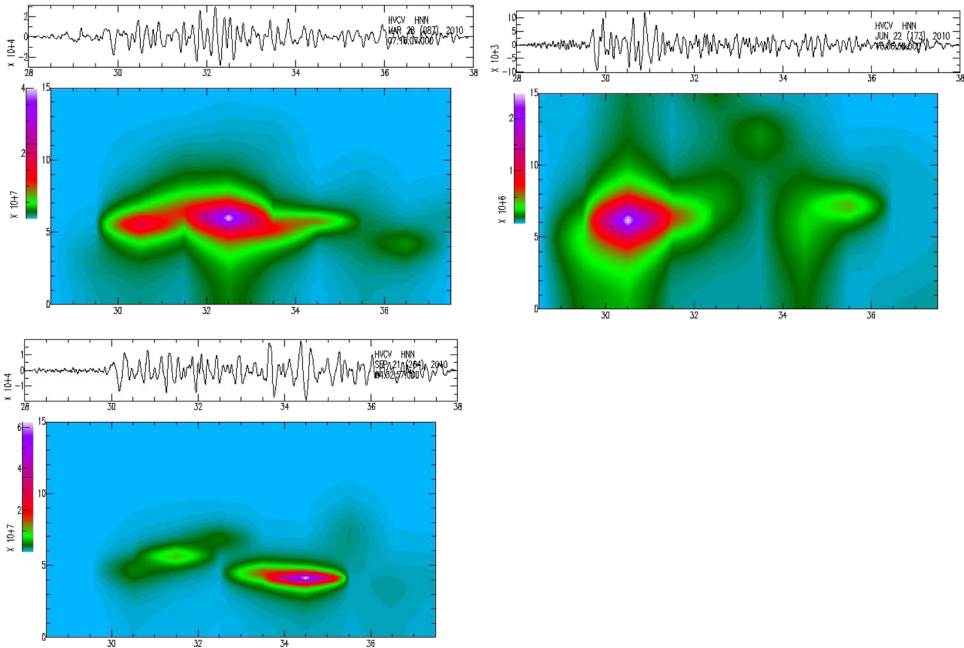
Figure 7. Spectrograms computed for the NS component at HVCV (right) for the three after-shocks (3/28, M4.4; 6/22, M3.3; 9/21, M4.4) shown in Figure 6 that were recorded at this station. Time in seconds.

band and its nadir-viewing and backward-viewing telescopes to acquire stereo image data with a base-to-height ratio of 0.6. The spatial resolution is 15 m in the horizontal plane. One nadir-looking ASTER VNIR (visible near-infrared) scene consists of 4,100 samples by 4,200 lines, corresponding to about 60-km-by-60 km ground area coverage.

The methodology used to produce the ASTER gDEM (global digital elevation model) involved automated processing of the entire 1.5-million-scene ASTER archive, including stereo-correlation to produce 1,264,118 individual scene-based ASTER DEMs, cloud masking to remove cloudy pixels, stacking all cloud-screened DEMs, removing residual bad values and outliers, averaging selected data to create final pixel values, and then correcting residual anomalies before partitioning the data into 1°-by-1° tiles.

The ASTER gDEM is in GeoTIFF format with geographic lat/long coordinates and a 1 arc-second (30 m) grid of elevation postings. It is referenced to the WGS84/EGM96 (World Geodetic System 1984/Earth Gravitational Model 1996) geoid. Pre-production estimated accuracies for this global product were 20 meters at 95% confidence for vertical data and 30 meters at 95% confidence for horizontal data. Initial validation studies concluded that the ASTER gDEM generally meets the pre-production accuracy predications, but results do vary and include areas where gDEM accuracy does not meet the pre-production estimates.

We employ a two-step process to display the ASTER gDEM for the Port-au-Prince region. The dataset includes elevation values ranging from -15 m to 3116 m.

The first step is to translate the data values into the 0 to 255 (byte) range standard to monitors and other graphics displays. The translation from data values to display values used here is a 2% linear stretch. This stretch uses a histogram of the dataset, and sets a floor and a ceiling at 2% and 98% of the dataset respectively. Data values below and above these values are assigned display values of 0 and 255, respectively. Because this is a linear stretch, the remaining 254 display values are distributed evenly across the data range. Data values are then binned accordingly and assigned to their corresponding display values.

The second step is to apply a color map to the display values. The output from the first step yields a picture whose elements use the full displayable range of values from 0 (black) to 255 (white). Features of a displayed dataset can be more effectively visualized by assigning colors rather than a gray scale. In color-mapping a grey-scale image, a color is assigned to each of the display values from 0 to 255. The exact mapping of each 0 to 255 display value to a specific color is commonly called a "color table." The color table used here is EOS-B, which is a blue (display value 0) to dark red (display value 255) gradual rainbow with 25 darker bars evenly spaced in the range.

To classify terrain units we consider the contoured topographic values together with V_{S30} values determined at 34 sites using the MASW method (Cox et al. 2011). Filtering small-scale topographic features that are not considered statistically significant, we use object-oriented analysis to identify the boundary between mountains (NEHRP class B) and alluvial fan terrains (NEHRP class C) and between the alluvial fan terrain and basin/near-shore terrain (NEHRP class D; Figure 8, see Yong et al. 2011 for detail). Although the object primitives reveal finer structure within the valley, we are not able to distinguish between finer scale terrain types that correlate significant variations in V_{S30} or estimated site response. Our final site characterization map, based on the conventional V_{S30} proxy, thus provides a first-order characterization based on available data.

The site characterization map shown in Figure 8 captures only the variability in near-surface geotechnical properties that are expected to control sediment-induced amplification of ground motions. To delineate the topographic features that are associated with amplification, we first turn to the observed damage distribution to extend our site response results, which quantify observed amplification at just two stations.

Before we consider the correspondence between damage and small-scale topography, we make a few general remarks about the damage pattern based on field observations. As noted, the extent of the damage was clearly largely due to high structural vulnerability. Even catastrophic damage cannot be taken as an indication of high intensities. For example, a direct eyewitness survey revealed that, in the well-built commercial structure shown in Figure 9a, shaking severity did not exceed modified Mercalli Intensity (MMI) V-VI. The buildings on both sides of this structure collapsed catastrophically. Similarly, the house shown in Figure 9b, which can reasonably be assumed to be Masonry type C (ordinary workmanship, no extreme weaknesses), sustained only very minor, surficial cracks, and some toppling of small objects, indicating MMI VI. Many structures, including a school building directly adjacent to the house, sustained catastrophic damage or collapse.
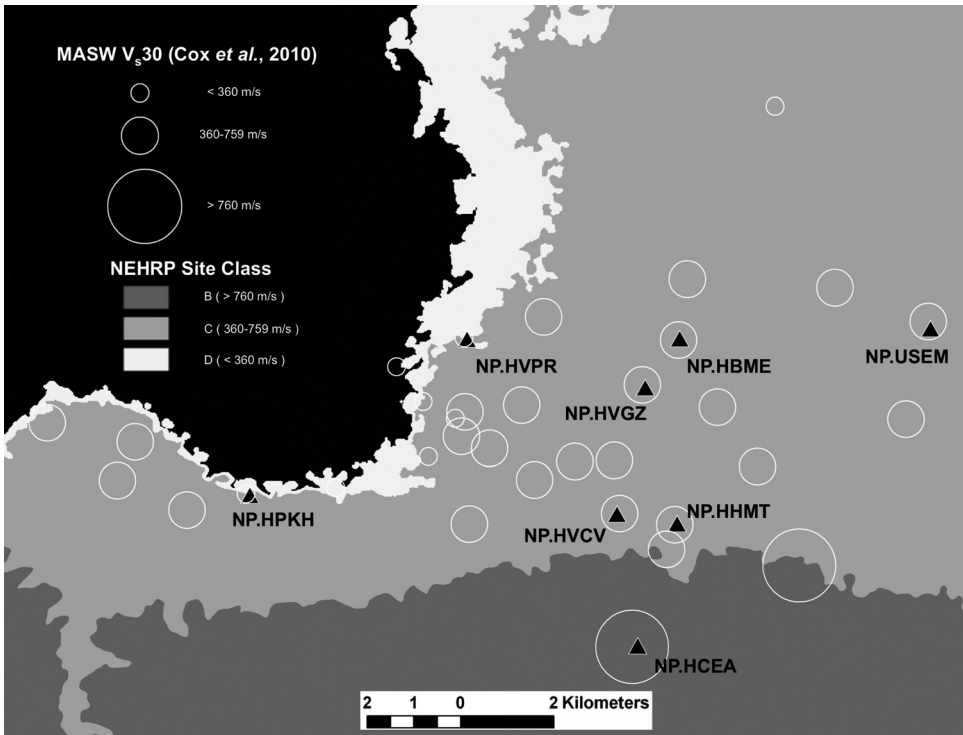
Figure 8. First-order site characterization map for the Port-au-Prince region determined from topographic analysis. Open circles indicate V_{S30} results (Cox et al. 2011); triangles are recording sites. See Yong et al. 2011.

Figure 9. (a) A good-quality commercial structure in which MMI V-VI is estimated based on an eyewitness interview; (b) a private home, masonry C construction, for which MMI VI is estimated. The structures on both sides of the structure shown in 8a collapsed catastrophically, as did a school building adjacent to the house shown in 8b.

Development of a reliable MMI map will therefore require collection and analysis of detailed surveys to assess intensities in well-built structures. It is possible, based on the small number of surveys conducted during our field investigations, that shaking throughout much of Port-au-Prince did not exceed MMI VI. It is therefore further possible that the distribution of damage throughout most of the city is primarily a reflection of the distribution of structural vulnerability.

The increasing availability of high-quality satellite data now allows for rapid damage assessments to be made from remote-sensing imagery. For example, in the immediate aftermath of the earthquake, scientists at the German Aerospace Center (DLR) collected, processed, and analyzed radar and optical data to develop a damage map for the city (http://www.dlr.de/en/desktopdefault.aspx/tabid-6213/10205_read-220). The DLR map assesses damage within grid cells 250-m square according to the percentage of damaged buildings: <10%, 10–40%, and >40% (Figure 2). Focusing on the sheet that covers the foothill ridge (Figure 10), one finds significant variability of damage.

In the southern metropolitan Port-au-Prince region, damage was generally less severe than in the rest of the city. This part of the city is generally more affluent, so structures are generally of better quality: Masonry C or in some cases B (well-built masonry, not specifically designed to reduce lateral forces), whereas poor-quality masonry (Masonry D) is prevalent throughout much of the city. However, there has been an absence of effective, enforced land-use planning in Haiti; shantytowns characterized by extremely poor construction have developed throughout the city, including within the relatively affluent southern foothills. The distribution of damage, even in this region, is thus expected to reflect a
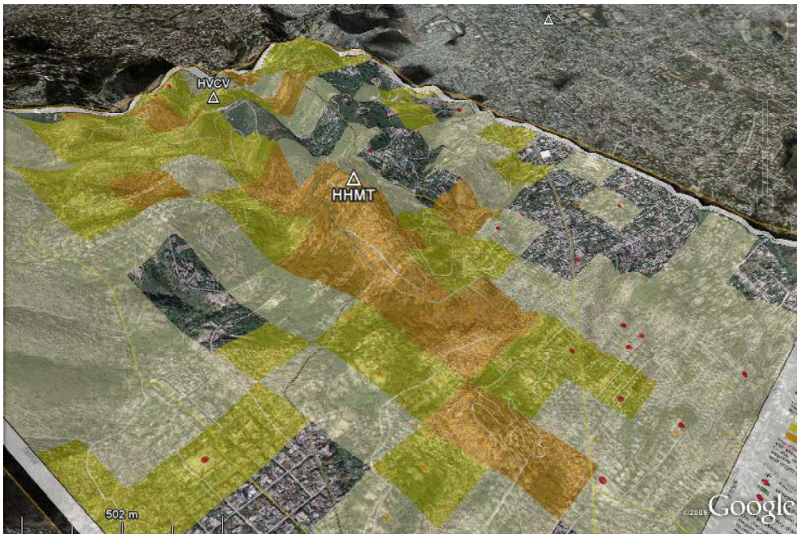

Figure 10. Damage in the southern metropolitan Port-au-Prince region draped over topography (x3 vertical exaggeration). Stations HVCV and HHMT (white trianges) are located along a narrow, roughly east-west trending ridge. (Same color scale as Figure 2).

number of different factors beyond ground motion severity. With this caveat in mind we explore the correspondence between the distribution of damage and topography.

Notwithstanding the expectation that the damage distribution is a coarse and imprecise indication of the shaking distribution, the draped damage distribution (Figure 10) reveals a close correspondence between the band of high damage and the narrow foothill ridge. Topographic profiles cutting across the ridge at the locations of HHMT and HVCV (Figure 11) further illustrate this correspondence. At HVCV, the band of high damage extends over a pair of sub-parallel ridges. At HHMT damage is low in the hills above the ridge, increasing significantly at the base of the ridge. Damage appears to drop to the north of HHMT, but there were few structures on the steep hillside immediately north of the hotel. The hotel complex itself included two multi-story structures built against the hillside; one building survived the earthquake, the other collapsed catastrophically.

In summary, the observed damage pattern suggests that mainshock ground motions were significantly amplified not only at the two ridge-peak locations for which we can quantify site response, but rather, in keeping with theoretical prediction (e.g., Sanchez-Sesma 1985) were generally amplified along the ridge shown in Figure 10.

Using a topographic map we can delineate the extent of the ridges that are associated with significant weak-motion amplification. No general method has been developed to map topographic features associated with significant amplification. Indeed it remains within the purview of active research to identify features that are significant for ground motions. For Port-au-Prince, the results could be combined in a map of PGA (or spectral) amplification. Our results indicate weak motion amplification factors of 1.8 for NEHRP site class C sites and 2.5–3 for sites on the ridge. The results further indicate weak motion PGA acceleration of 2.1 for NEHRP class D sites, but this is not well constrained.

The damage distribution for the Haiti earthquake suggests a general correlation of damage with small-scale topographic features. For example, the damage distribution in the
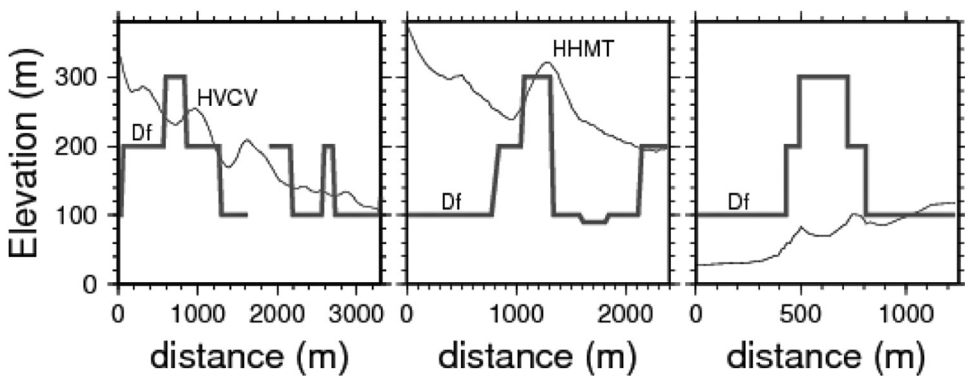

Figure 11. Topographic profiles running southwest-northeast through station (a) HVCV and (b) HHMT. Also shown is (c) a profile running north-south from the airport (discussed in a later section). Scaled damage factor, Df, shown on each panel (heavy gray lines: 300, 200, and 100 correspond to orange, yellow, and tan in Figure 2).
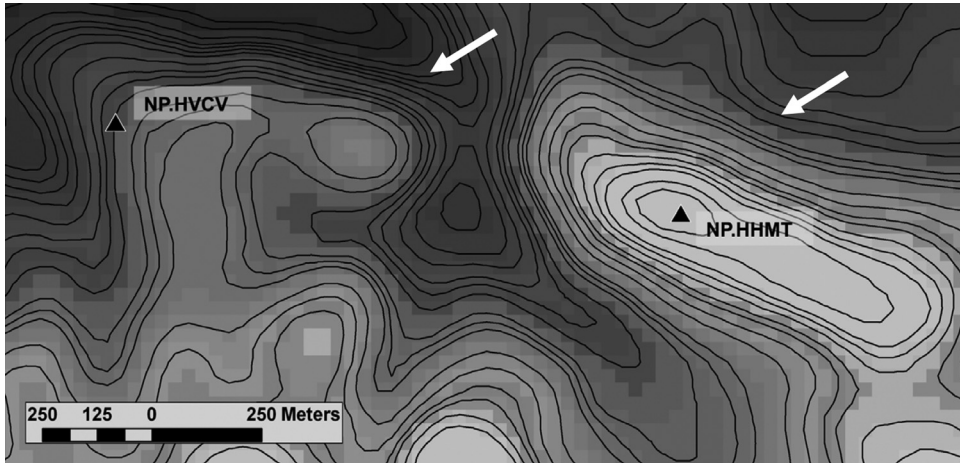
Figure 12. Topographic contours of ridges inferred to correspond to significant amplification of ground motion. The base of the eastern ridge can be cleanly delineated by the indicated contour line.

western/central Port-au-Prince metropolitan region reveals higher damage on hills to the east of the more flat-lying downtown region (Figure 13a). The band of high damage in the foreground of Figure 13a is the downtown area, where sediments are relatively soft compared to other parts of the city. The topography (and likely the V_{S30} values) increases to the east of this region; as expected, less damage is observed in this region. We note, however, a zone of increased damage farther east/southeast, coinciding with increased small scale topographic roughness. Similarly, damage was light in the immediate vicinity of the airport, which is northeast of central Port-au-Prince (see Figure 2), but significantly higher on foothills to the immediate south (Figure 13b). The profiles shown in Figure 11 follow roughly along the road indicated in Figure 13b. Although the DLR damage distribution does not provide a damage estimation between the point indicated and the airport, we estimate a continuation of $Df = 1$ in this region based on direct assessment.

CONCLUSIONS

We have used available ground motion and damage data together with terrain analysis based on a high-resolution, satellite-based ASTER-based gDEM and available V_{S30} results (Cox et al. 2011) to develop a first-order site characterization map for Port-au-Prince, Haiti. This map is based on a small fraction of the data that is available for a well-instrumented, well-studied region such as southern California (e.g., Wills et al. 2000, Field et al. 2000), but captures the large-scale terrain units that correspond to distinguishable differences in estimated V_{S30} and observed site response. Our results further reveal that the most significant observed site-related weak-motion amplification effects were associated with topographic amplification along steep foothill ridges rather than sediment-induced amplification due to low impedance near-surface layers.
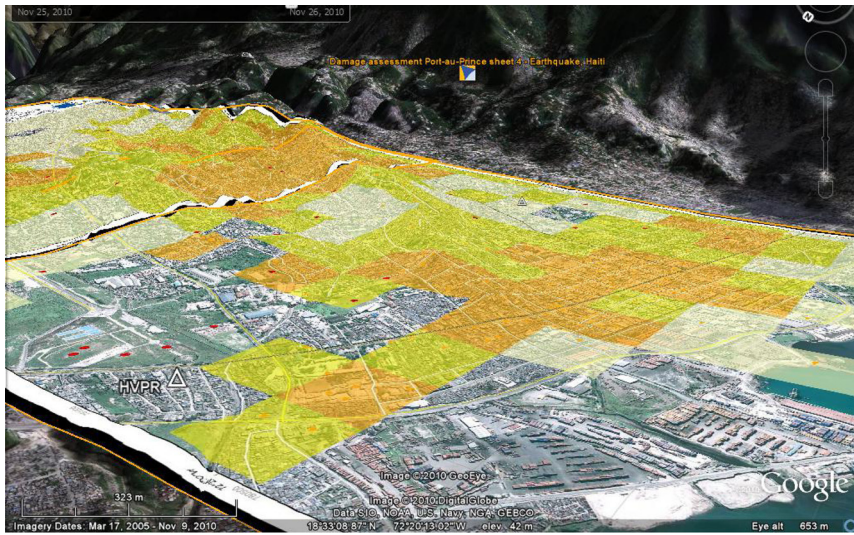
(a)

(b)

Figure 13. (a) The DLR damage distribution for the west/central Port-au-Prince metropolitan region, to the north of the region shown in Figure 10. (b) Damage distribution looking roughly southeast from airport (foreground) towards low foothills immediately to the south. Damage was light in the vicinity of the airport, but significantly higher in the adjacent hills.

Recordings of more and larger earthquakes will potentially improve site response estimates. All of our site response estimates are derived from weak-motion data. During strong ground motion, non-linearity of soft sedimentary layers has been shown to reduce the

severity and shift the predominant periods of sediment-induced amplification (e.g., Aki 1993). Very little work has been done to explore non-linearity of topographic amplification. We note, however, that the damage distribution provides a confirmation that amplification is significant for strong as well as weak ground motion.

A growing number of case studies have demonstrated that topographic features can amplify ground motions significantly at frequencies of engineering concern (e.g., Hartzell et al. 1994, Spudich et al. 1996, Bouchon et al. 1996, Assimaki et al. 2005, Lee et al. 2009, Pischiutta et al. 2010). However, while a number of proxy-based methods have been determined to map out the impedance of near-surface layers (e.g., Wills et al. 2000, Yong et al. 2008, Allen and Wald 2009), there is no similarly systematic, simple way to characterize topography and to develop associations between topographic effects and amplification. Allen and Wald (2009) develop a site characterization method based on maximum slope, but they assume a one-to-one mapping between steepness and V_{S30}. That is, they assume that amplification is controlled by V_{S30}, and do not explore the possibility of topographic amplification. Topographic amplification is controlled by two- if not three-dimensional topographic structure (e.g., Assimaki et al. 2005, Lee et al. 2009). Thus a more sophisticated method to characterize topography, beyond a single slope parameter, will be required to develop associations between topography and amplification. Terrain classification methods have recently been developed (e.g., Iwahashi and Pike 2007, Yong et al. 2010); however, the development of associations between terrain and amplification remains in its infancy (e.g., Yong et al. 2009).

Effective microzonation for the city of Port-au-Prince will need to incorporate both topographic and sediment-induced amplification effects. Observed amplifications at foothill ridge stations HHMT and HVCV reveal significant variability for both PGA and spectral response, but reach factors of 4–5 over frequencies between a few and 10 Hz. This frequency range corresponds roughly to the natural period of one- to five-story structures; structures of this size were, and are expected to continue to be, ubiquitous in Port-au-Prince.

ACKNOWLEDGMENTS

REFERENCES

Aki, K., 1993. Local site effects on weak and strong ground motion, *Tectonophysics* **218**, 933–111.

Allen, T. I., and Wald, D. J., 1984. On the use of high-resolution topographic data as a proxy for seismic site conditions (V_{S30}), *Bull. Seism. Soc. Am.*, **99**, 935–943, DOI: 10.1785/0120080255.

Anderson, J. G., and Hough, S. E., 1984. A model for the shape of the Fourier amplitude spectrum of acceleration at high frequencies, *Bull. Seism. Soc. Am.* **74**, 1969–1993.

Assimaki, D., Gazetas, G., and Kausel, E., 2005. Effects of local soil conditions and topographic aggravation of seismic motion: Parametric investigation and recorded field evidence from the 1999 Athens earthquake, *Bull. Seism. Soc. Am.* **95**, 1059–1089.

Borcherdt, R. D., and Gibbs, J. F., 1970. Effects of local geology on ground motion near San Francisco Bay, *Bull. Seism. Soc. Am.*, **60**, 29–61.

Bouchon, M., Schultz, C. A., and Toksoz, M. N., 1996. Effect of three-dimensional topography on seismic motion, *J. Geophys. Res.* **101**, 5835–5846.

Cox, B. R., Bachhuber, J., Rathje, E., Wood, C. M., Kottke, A., Green, R., and Olson, S., 2011. Shear-wave-velocity and geology-based seismic microzonation of Port-au-Prince, Haiti, *Earthquake Spectra* **27**, this issue.

Cranswick, E., 1988. The information content of high-frequency seismograms and the near-surface geologic structure of "hard rock" recording sites, *Pure App. Geophys.* **128**, 333–363, DOI: 10.1007/BF01772604.

Field, E. H., 2000. A modified ground-motion attenuation relationship for Southern California that accounts for detailed site classification and a basin-depth effect, *Bull. Seism. Soc. Am.* **90**, S209–S221.

Hartzell, S. H., Carver, D. L., and King, K. W., 1994. Initial investigation of site and topographic effects at Robinwood Ridge, California, *Bull. Seism. Soc. Am.* **84**, 1336–1349.

Hough, S. E., 1995. Observational constraints on earthquake source scaling: understanding the limitsin resolution, *Tectonophysics* **261**, 83–96.

Hough, S. E., Friberg, P. A., Busby, R., Field, E. F., Jacob, K. H., and Borcherdt, R. D., 1990. Sediment-induced amplification and the collapse of the Nimitz freeway, *Nature* **344**, 853–855.

Hough, S. E., Altidor, J. R., Anglade, D., Benz, H., Ellsworth, W., Given, D., Hardebeck, J., Janvier, M. G., Maharrey, J. Z., Mazabraud, Y., McNamara, D., de Lepinay, B. M., Meremonte, M., Mildor, B. S-L., Prepetit, C., and Yong, A., 2010. Localized damage associated with topographic amplification during the 12 January 2010 M7.0 Haiti earthquake, *Nature Geoscience* **3**, 778–782.

Joyner, W. B., 2000. Strong motion from surface waves in deep sedimentary basins, *Bull. Seism. Soc. Am.* **90**, S95–S112.

Iwahashi, J., and Pike, R. J., 2007. Automated classifications of topography from DEMs by an unsupervisednested-means algorithm and a three-part geometric signature, *Geomorphology*, **86**, 409–440.

Lee, S. J., Chan, Y. C., Komatitsch, D., Huang, B. S., and Tromp, J., 2009. Effects of realistic surface topography on seismic ground motion in the Yangminshan region of Taiwan based on the spectral-element method and LiDAR DTM, *Bull. Seism. Soc. Am.* **99**, 681–693.

Paolucci, R., 2002. Amplification of earthquake ground motion by steep topographic irregularities, *Earthq. Eng. and Struct. Dyn.*, **31**, 1831–1853.

Pischiutta, M., Cultrera, G. Caserta, A. Luzi, L. and Rovelli, A., 2010. Topographic effects on the hill of Nocera Umbria, central Italy, *Geophys. J. Int.* **182**, 977–987.

Sanchez-Sesma, F. J., 1985. Diffraction of elastic SH waves by wedges, *Bull. Seism. Soc. Am.* **75**, 1435–1446.

Singh, S. K., Mena, E., and Castro, R., 1988. Some aspects of source characteristics of the 19 September 1985 Michoacan earthquake and ground motion amplification in and near Mexico City from strong motion data, *Bull. Seism. Soc. Am.* **78**, 451–477.

Spudich, P., Hellweg, M., and Lee, W. H. K., 1996. Directional topographic site response at Tarzana observedin aftershocks of the 1994 Northridge, California earthquake: Implications for mainshock motions, *Bull. Seism. Soc. Am.* **86**, S193–S208.

Su, F., Aki, K., Teng, T., Zeng, Y., Koyanagi, S., and Mayeda, K., 1992. The relation between site amplification factor and surficial geology in central California, *Bull. Seism. Soc. Am.* **82**, 580–602.

Wills, C. J., Petersen, M., Bryant, W. A., Reichle, M., Saucedo, G. J., Tan, S., Taylor, G., and Treiman, J., 2000. A site-conditions map for California based on geology and shear-wave velocity, *Bull. Seism. Soc. Am.* **90**, S187–S208.

Yong, A., Hough, S. E., Abrams, M. J., Cox, H. M., and Wills, C. J., 2008. Quantification of site characterization from remote-sensing data, *Bull. Seism. Soc. Am.* **98**, 2679–2693.

Yong, A., and Hough, S. E., 2009. Topographic site response at hardrock sites, *Eos Trans.* **90**, 52, Fall Meet. Suppl. Abstract (S41E-03).

Yong, A., Hough, S. E., Braverman, A., and Iwahashi, J., 2010. A terrain-based V_{S30} estimation map of the contiguous United States, *Seism. Res. Lett.* **81**, 294.

Yong, A., Hough, S. E., Cox, B. R., Rathje, E. M., Bachuber, J., Huslander, R., Christiansen, L., and Abrams, M. J., 2011. Terrain classification of ASTER gDEM for a preliminary seismic micronization map of Port-au-Prince, Haiti, using pixel- and object-based imaging analysis methods, *Programmatic Eng. and Remote Sensing*, in press.